

# Integrated Polarization-Analyzing CMOS Image Sensor for Detecting the Incoming Light Ray Direction

Mukul Sarkar, *Student Member, IEEE*, David San Segundo Bello, *Member, IEEE*,  
Chris Van Hoof, *Member, IEEE*, and Albert J. P. Theuwissen, *Fellow, IEEE*

**Abstract**—A complementary metal–oxide–semiconductor (CMOS) image sensor used to detect the incoming light ray direction using polarization information is presented. The chip consists of an array of  $128 \times 128$  pixels, and each pixel is embedded with a metallic wire-grid micropolarizer. It occupies an area of  $5 \times 4 \text{ mm}^2$ , and it has been designed and fabricated in a 180-nm CMOS process. Extinction ratios of 6.3 and 7.7 were achieved in two different polarization sense regions. The Stokes parameters, which are needed to evaluate the degree of polarization (DOP) and electric-field vector intensity, are computed from the pixel with the micropolarizer oriented at  $0^\circ$ ,  $45^\circ$ , and  $90^\circ$ . We show that the variations in the DOP and the e-vector pattern with the incoming polarized light ray direction can be used as a directional reference source for autonomous agent navigation. We also show that the measurement results of ellipticity and azimuthal angles for the incoming light ray using the Stokes parameters can allow on-chip position detection based on the angle of the incoming light ray with little complexity. A very high correlation coefficient bigger than 0.94 was obtained between the measured and theoretical incoming light ray angles.

**Index Terms**—Complementary metal–oxide–semiconductor (CMOS) image sensors (CISs), micropolarizers, navigation, polarization.

## I. INTRODUCTION

NAVIGATION is essential in performing various living tasks. Based on cognitive mapping, navigation can be broadly classified into either geocentric or egocentric [1], [2]. In geocentric navigation, one uses its cognitive map and its orientation with respect to geocentric coordinates in order to set a course toward a goal. In this case, visual cues such as landmarks become very important to generate cognitive maps.

Manuscript received April 12, 2010; revised July 5, 2010; accepted September 7, 2010. Date of publication April 11, 2011; date of current version July 13, 2011. The Associate Editor coordinating the review process for this paper was Dr. Deniz Gurkan.

M. Sarkar is with the Electronic Instrumentation Laboratory, Delft University of Technology, 2628 Delft, The Netherlands (e-mail: m.sarkar@tudelft.nl).

D. San Segundo Bello and C. Van Hoof are with Imec, 3001 Leuven, Belgium (e-mail: David.SanSegundoBello@imec.be; Chris.VanHoof@imec.be).

A. J. P. Theuwissen is with Harvest Imaging, 3960 Bree, Belgium, and also with the Electronic Instrumentation Laboratory, Delft University of Technology, 2628 Delft, The Netherlands (e-mail: a.j.p.theuwissen@tudelft.nl).

Color versions of one or more of the figures in this paper are available online at <http://ieeexplore.ieee.org>.

Digital Object Identifier 10.1109/TIM.2011.2130050

Egocentric navigation, on the other hand, relies on path integration, where the movement cues of the navigator are continuously integrated. Humans navigate using geocentric navigation, whereas certain animals are known to use the egocentric form of navigation. The egocentric form of navigation is best suited for autonomous agents than the geocentric form as the latter would need to store and analyze visual cues, making the process cumbersome.

A path integration vector in the egocentric form of navigation is computed using the direction of travel and the distance traveled [3]. To determine the direction of travel, a reference direction is needed. The direction is then always expressed relative to the reference. In conventional autonomous agent navigation algorithms, the angle of travel is determined by capturing multiple images by a conventional camera and using complex image processing algorithms [4], [5]. The implementation of these algorithms needs very complex digital logic, and image processing requires high power consumption and high bus bandwidth [6]. This limits the design of miniature and low-power vision-based navigation systems.

An insect such as the Saharan desert ants (*Cataglyphis fortis*) uses the sun's movement to determine their direction of travel [3]. Since the movement of the sun is constant and equal to approximately  $1^\circ$  every 4 min, it serves as a very good directional reference. To determine the direction of travel, the ants use a celestial compass either based on direct sunlight (i.e., a sun compass) or the pattern of polarized sky light (i.e., polarization compass) [7]. This makes their navigation pattern completely independent of external visual cues.

To determine the position of the sun using direct sunlight, conventional analog sun position sensors can be used. These sensors measure the position of the sun by allowing the light from the sun to pass through a pinhole array and illuminate a certain region of an imaging array [8]. The position of the illuminated region is then used to compute the altitude and the direction of the sun with respect to the sensors. State-of-the-art digital sun sensors such as that in [9] use a centroid method to compute the angular position of the sun, whereas row profiling is used in a winner-takes-all (WTA) method proposed in [10]. The prerequisite of these sun sensors is that they need to see the sun, which is not very helpful in a cloudy day. Additionally, these sensors need an additional pinhole array and digital processors to compute the centroid of the obtained image.

The other compass used by insects is the polarization compass. Direct sunlight is always unpolarized. When this unpolarized light enters Earth's atmosphere, it collides with air molecules or is scattered because of fluctuations in air density. The light scattered by air molecules (i.e., perceived sky light) is partially polarized, which means that it is a combination of both unpolarized natural light and a linearly polarized component [11]. The pattern of the electric field vector (e-vectors) of sky light and the degree of polarization (DOP) are not constant over the sky and rather depend on the angle between the viewing direction and the position of the sun [12]. The variation in the DOP with the azimuthal position of the sun was experimentally observed in [11] and [13].

State-of-the-art polarization image sensors consist of a photodetector array such as a complementary metal-oxide-semiconductor (CMOS)/charge-coupled device sensor array and a single- or a multiaxis micropolarizer array to measure polarization information in real time [14], [15]. The micropolarizer can either be fabricated on a surface and bonded to a pixel array [15] or can be fabricated directly on the sensor array [16], [19]. For an EM wave to be absorbed by a wire grid, its wavelength should be larger than the pitch of the wire grid (i.e.,  $\lambda/d > 2$ , where  $\lambda$  is the wavelength, and  $d$  is the spacing between the wire grid) [17]. The visible spectrum wavelengths range from 300 to 720 nm, and thus, a wire-grid pitch of less than 300 nm is desired. With the scaling of CMOS technology, the distance between metal layers also scales, opening up the possibility of using them in a grid structure for the absorption of EM waves. The metallic wire grid has been shown to selectively transmit wavelengths [18]; however, they can also be used to detect polarization [19].

We have demonstrated a navigational sensor for autonomous agents to determine the direction of an incoming light ray using the e-vector pattern of the incoming polarized light ray [19]. The ellipticity angle of a Poincaré sphere, which is computed from the Stokes parameters, was shown to be correlated with the incoming polarized light ray direction. The Poincaré sphere, which is used to display the Stokes parameters, is characterized by ellipticity and azimuthal angles. In this paper, we present an extension of our previous work on incoming light ray direction detection, evaluating both the ellipticity and azimuthal angles for the incoming polarized light ray direction. We also show that, besides the e-vector pattern, the changes in the DOP also serves as a good tool to determine directional information. A full-fledged navigational algorithm employing the e-vector and the DOP of polarized light has not been explored in sensors to our knowledge, although this principle is very common in insects.

Section II covers the theory behind the polarization of light. Section III describes the designed image sensor with two polarization sense regions with micropolarizers created using a metallic wire grid. Section IV presents the performance of the metallic wire-grid micropolarizers along with the experimental results of the measured azimuthal and ellipticity angles and the DOP for variations in polarized incoming light ray directions. Section V details the conclusions, and an outline of the future work is presented.

## II. THEORY

### A. Stokes Parameters and the DOP

EM radiation travels as transverse waves, i.e., waves that vibrate in a direction perpendicular to their direction of propagation. Polarization is the distribution of an electric field in a plane normal to the propagation direction, which is a phenomenon peculiar to transverse waves. In an unpolarized or a randomly polarized EM wave, the orientation of the e-vector changes randomly.

The mathematical representation of a plane wave propagating in the  $z$ -direction is given by

$$E = E_0 \cos(kz - \omega t + \varphi_0) \quad (1)$$

where  $E_0$  is the amplitude,  $k$  is the propagation (or wave) constant ( $k = 2\pi/\lambda$ ),  $\omega$  is the circular frequency ( $\omega = kc = 2\pi c/\lambda$ ), and  $\varphi_0$  is the initial phase.

The polarization state of the EM wave can be conveniently described by the Stokes parameters, which were developed by G.G. Stokes in 1852. The four Stokes parameters  $S_0$ ,  $S_1$ ,  $S_2$ , and  $S_3$ , which are expressed as a function of electric field strength, are shown in

$$\begin{aligned} S_0 &= E_{x0}^2 + E_{y0}^2 \\ S_1 &= E_{x0}^2 - E_{y0}^2 \\ S_2 &= 2E_{x0}E_{y0} \cos(\nabla\varphi) \\ S_3 &= 2E_x E_y \sin(\nabla\varphi) \end{aligned} \quad (2)$$

where  $E_{x0}$  is the field strength of the parallel polarized light,  $E_{y0}$  is the field strength of the perpendicular polarized light, and  $\nabla\varphi$  is the phase difference between the parallel and the perpendicular polarized light.

The Stokes parameters correspond to the measurement of the intensity of the light ray passing through different filter arrangements. The Stokes parameters used for this paper are modified [16], as shown in

$$\begin{aligned} S_0 &= I_{90^\circ} + I_{0^\circ} \\ S_1 &= I_{90^\circ} - I_{0^\circ} \\ S_2 &= I_{45^\circ} - I_{0^\circ} \\ S_3 &= I_{90^\circ} - I_{45^\circ} \end{aligned} \quad (3)$$

where  $I_{0^\circ}$  is the intensity of light after passing through a horizontal linear polarizer,  $I_{90^\circ}$  is the intensity after a vertical linear polarizer, and  $I_{45^\circ}$  is the intensity after a linear polarizer is placed at  $45^\circ$ .

The Poincaré sphere shown in Fig. 1 is used to display the three independent Stokes parameters  $S_1$ ,  $S_2$ , and  $S_3$  as points on or inside the sphere.

In Fig. 1,  $\psi$  is the polarization azimuthal angle, and  $\chi$  is the ellipticity angle. The surface of the Poincaré sphere is commonly used to give a pictorial representation of all the possible polarization states of completely polarized light. The

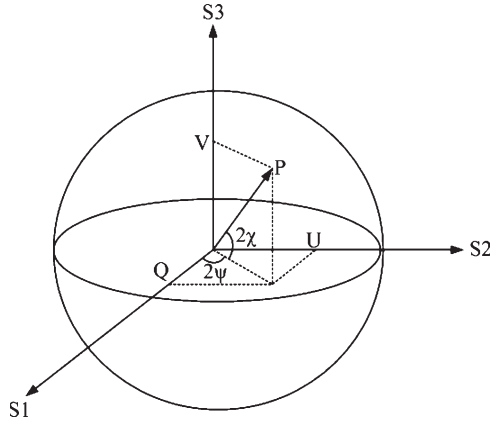


Fig. 1. Poincare sphere representation.

polarization azimuthal angle  $\psi$  and the ellipticity angle  $\chi$  can be expressed in terms of the Stokes parameters as

$$\begin{aligned} \sin 2\chi &= \frac{S_3}{\sqrt{S_1^2 + S_2^2 + S_3^2}} \\ \tan 2\psi &= \frac{S_2}{S_1}. \end{aligned} \quad (4)$$

Since the electric field of an EM wave polarized by scattering consists of polarized and unpolarized components, the percentage of the electric field of light, which is polarized compared with the electric field of total incident light, is defined as the DOP. The DOP is represented in the Poincaré sphere by vector  $P$  in Fig. 1. In terms of Stokes parameters, the DOP of a light beam is expressed as

$$DOP = \frac{\sqrt{S_1^2 + S_2^2 + S_3^2}}{S_0}. \quad (5)$$

In a linearly polarized light beam, circular polarization and elliptical polarization do not usually occur; thus, its DOP is often referred to as the degree of linear polarization (DOLP). The DOLP of the light beam is defined by

$$DOLP = \frac{S_1}{S_0}. \quad (6)$$

The DOP is also related to the maximum and minimum transmitted intensity values [20], as shown in the following:

$$DOP = \delta(x, y) = \frac{I_{\max}(x, y) - I_{\min}(x, y)}{I_{\max}(x, y) + I_{\min}(x, y)} \quad (7)$$

where  $I_{\max}$  and  $I_{\min}$  are the maximum and minimum transmitted intensity values for the pixel at coordinates  $x$  and  $y$ . The maximum transmittance in a polarizer is achieved when the polarization axis is parallel to the polarization of incoming light, whereas the minimum transmittance occurs when the polarization axis is perpendicular to the polarization of incoming light.

### III. SENSOR DESCRIPTION

We have realized a polarization-analyzing CMOS image sensor (CIS) using an embedded metallic wire-grid micropolar-

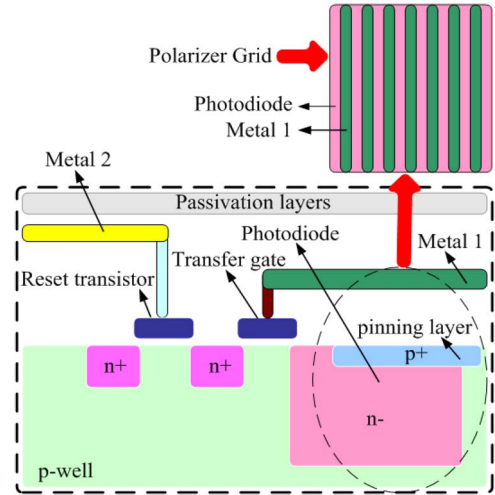


Fig. 2. Pixel cross section and the implemented wire-grid polarizer.

TABLE I  
SENSOR SPECIFICATIONS

Process	0.18 $\mu\text{m}$ 1 P3M UMC CIS process
On-chip Polarizer	Line/Space = 0.24 $\mu\text{m}$ / 0.24 $\mu\text{m}$ (0.48 $\mu\text{m}$ pitch)
Active imager size	3.2 mm(H) x 3.2 mm(V)
Chip Size	4 mm(H) x 5 mm(V)
Active pixels	128 x 128
Pixel size	25 $\mu\text{m}$ x 25 $\mu\text{m}$
Shutter type	Global shutter
Maximum data rate/master clock	64 MPS / 32 MHz
Supply voltage	1.8V

izer, which is made using metal layers available with standard CMOS technology. The image sensor consists of an array of 128  $\times$  128 pixels. It occupies an area of 5  $\times$  4 mm<sup>2</sup>, and it has been designed and fabricated in the 180-nm CIS process from United Microelectronics Corporation. The embedded wire-grid micropolarizer in each pixel is realized with the first metal layer of the process on top of a pinned photodiode (p<sup>+</sup>/n<sup>-</sup>/p-sub). The linear wire-grid polarizer has a line/space of 240/240 nm (i.e., a pitch of 480 nm), as shown in Fig. 2.

Table I shows the sensor specifications. The sensor architecture is shown in Fig. 3.

The chip is divided into four main blocks. The first one is a pixel array with photodiodes and associated circuitry for analog computations, which occupies most of the chip area. Each pixel contains a pinned photodiode and 32 transistors to perform low-level image processing. The size of the photodiode is 10  $\mu\text{m}$   $\times$  10  $\mu\text{m}$ , which corresponds to a 16% pixel fill factor. In this paper, we focus on the polarization sensing ability of the sensor; thus, the low-level image processing will not be discussed. Second, placed below the pixel array is an analog readout circuit. The analog readout circuit consists of column-level circuits to perform double differential sampling, an output amplifier, a buffer, and a column shift register. The analog output provides analog voltage at each pixel. Third, placed at the top is a digital readout circuit. The digital readout circuit consists of a 7-b counter and a column shift register. The 7-b counter is used to count the number of active high pixels in each



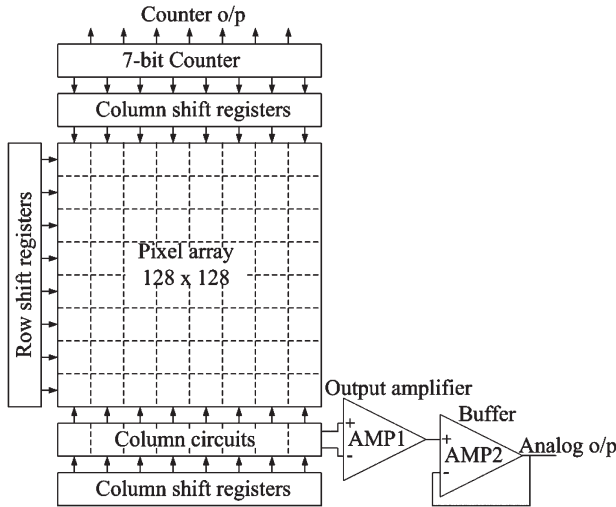


Fig. 3. Sensor architecture.

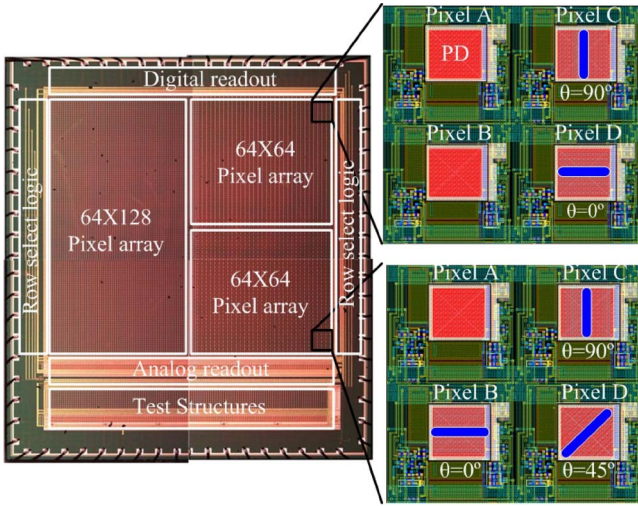


Fig. 4. Sensor regions with different polarizing angles.

row. Finally, the left side is dedicated to row select logic and timing control blocks to address each row of pixels sequentially.

The array of  $128 \times 128$  pixels was split into the following three regions, as shown in Fig. 4.

- 1) A  $64 \times 128$  array without a metal grid used for normal imaging applications;
- 2) A  $64 \times 64$  array (i.e., sense region 1) consisting of  $2 \times 2$  pixel arrays, where two pixels (A and B) measure intensity, whereas the other two measure  $0^\circ$  (D) and  $90^\circ$  (C) polarized intensity, respectively;
- 3) A  $64 \times 64$  array (i.e., sense region 2) consisting of  $2 \times 2$  pixel arrays where one pixel records the intensity of light (A), whereas the other three record  $0^\circ$  (B),  $45^\circ$  (C), and  $90^\circ$  (D), polarized intensity.

Additional pixel sensitivity to  $45^\circ$  polarized light in sense region 2 is used to compute the Stokes parameters. The pixels dedicated to sense the intensity in regions 1 and 2 are used to normalize the data obtained from the pixels sensitive to the polarization directions.

The full pixel size is  $25 \mu\text{m} \times 25 \mu\text{m}$  and is comprised of a pinned photodiode, an analog comparator, two banks of

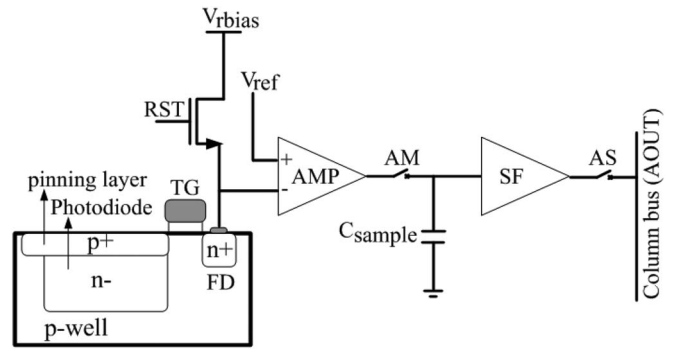


Fig. 5. Simplified pixel architecture.

analog memory devices and two six-transistor static random access memory cells to store an in-pixel binarized value. In-pixel binarization is not discussed in this paper. Fig. 5 shows the signal chain for the photodiode voltage transfer from the transfer gate  $TG$  to the sampling capacitor  $C_{\text{sample}}$  for the designed pixel. Two such sampling capacitors are available in the pixel to sample photodiode voltage at different time instances. Switch  $AM$  allows access to the sampling capacitor. The buffer amplifier  $AMP$  located between the photodiode and the sampling capacitor  $C_{\text{sample}}$  serves two functions: amplification and comparison.

The image capture begins with a reset of the pixel by switching the  $RST$  switch on. The voltage at the floating diffusion node  $FD$  is then set to the reset voltage  $V_{r\text{bias}}$ . The reset is global in nature for the entire pixel array. After the reset, the photodiode starts accumulating the photogenerated charge. The time spent accumulating the charge is referred to as the integration time or the exposure period. At the end of the integration time, the accumulated charge is transferred to  $FD$ .

The voltage change at the  $FD$  node due to the transferred photocharge is sampled onto the sampling capacitor  $C_{\text{sample}}$  when switch  $AM$  conducts. The source follower  $SF$  loads the column bus  $AOUT$  via the analog row selection switch  $AS$  with the signal sampled on the sampling capacitor during readout of the pixel.

#### IV. PERFORMANCE ANALYSIS

##### A. Measurement Setup

Fig. 6(a) shows the specially designed experimental platform used to characterize the image sensor. Two Xilinx Virtex-II pro development boards [21] are used to generate clocks and control signals for the image sensor, an analog-to-digital converter (ADC), and a frame grabber. An external ADC is used to digitize the output signal of the image sensor. The ADC used is a 12-b ADC from analog devices (AD9821) [22]. The frame grabber used in the measurement setup is an IC-PCI frame grabber installed in a personal computer (PC). A LabVIEW user interface from DALSA was used to analyze the image data.

The sensor was quantitatively tested for conversion gain, sensitivity, dark currents, dynamic ranges, and signal-to-noise ratios. The measured performance parameters of the image sensor are summarized in Table II.

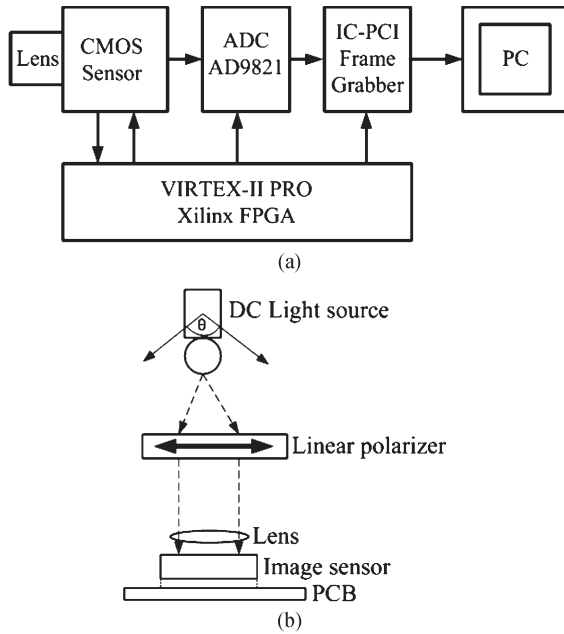


Fig. 6. Measurement setup.

TABLE II  
SENSOR PERFORMANCE CHARACTERISTICS

Parameters	Measured
Sensitivity	13.94 mV/ms
SNR	33 dB
Conversion gain	11.3 $\mu\text{V}/e^-$
Read Noise (CDS)	18 $e^-$ at pixel level
Dark Current @ RT	18pA/cm <sup>2</sup>
Dynamic Range (CDS)	68 dB at pixel level
Sense Node Cap.	14.5 fF
Full well	43186 $e^-$

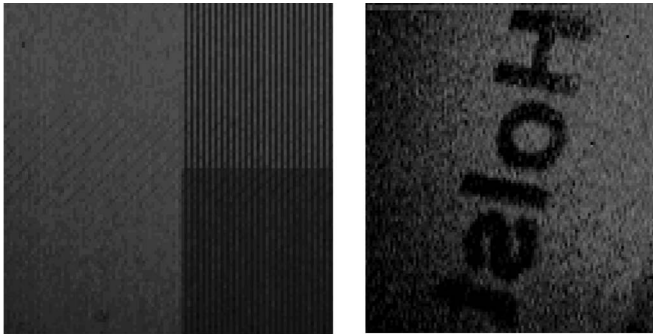


Fig. 7. (Left) Sample images. (Right) Transmission photograph of the wire-grid line array Holst text.

Fig. 7 shows some sample images obtained using the image sensor. The image on the left is the transmission image showing the attenuation of light in the regions where the photodiode has an integrated metallic wire-grid polarizer. Sense region 2 has three pixels with a wire-grid polarizer; thus, the attenuation of light is greater compared with sense region 1. The image on the right is a sample text.

Due to measurement setup constraints, it was not possible to measure the variations of the DOP and the e-vector with respect to the angular position of the sun under an open sky. The experimental setup shown in Fig. 6(b) was built for

indoor measurements using a direct-current (dc) light source. The sensor is illuminated with polarized light obtained by passing the light from the dc light source through an external linear polarizer. The corresponding analog outputs of the pixels sensitive to 0°, 45° and 90° in the polarization sense regions are recorded. These measurements are then sent to the PC for further processing. For the first version of the sensor, the Stokes parameters were computed off-chip to have a proof of concept. The circuits required for the computation of Stokes parameters and other digital processing for the implementation of the algorithm can easily be integrated on-chip.

An average value of the intensity of the pixel sensitive to 0° and 90° in sense region 1 and 0°, 45°, and 90° in sense region 2 is computed for 30 frames using the following:

$$p_{\text{avg}}(\text{With a linear polarizer})(x, y) = \frac{1}{N} \sum_{n=1}^N p_n(x, y) \quad (8)$$

where  $p_n(x, y)$  is the measured pixel intensity,  $x$  and  $y$  correspond to the row and column address of the pixel in the sensor array, and  $N$  is the number of frames selected. At the beginning of the experiment, the mean of an array of  $20 \times 20$  pixels without the linear polarizer is calculated as in (9). The result is used as a normalization factor given by

$$p_{\text{avg}}(\text{Without a linear polarizer})(x, y) = \frac{1}{XYN} \sum_{n=1}^N \sum_{x=0}^{X-1} \sum_{y=0}^{Y-1} p_n(x, y) \quad (9)$$

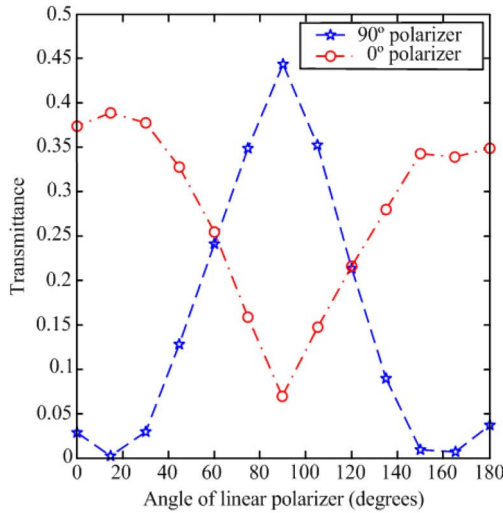
where  $X$  and  $Y$  are the pixel array dimensions, and  $N$  is the total number of frames used to compute the mean. Normalized intensity is then obtained by dividing mean pixel intensity with the linear polarizer [see (8)] by the mean pixel intensity without the linear polarizer [see (9)], as shown in

$$\text{Normalized } p_{\text{avg}}(x, y) = \frac{\left( \frac{1}{N} \sum_{n=1}^N p_n(x, y) \right)}{\left( \frac{1}{XYN} \sum_{n=1}^N \sum_{x=0}^{X-1} \sum_{y=0}^{Y-1} p_n(x, y) \right)} \quad (10)$$

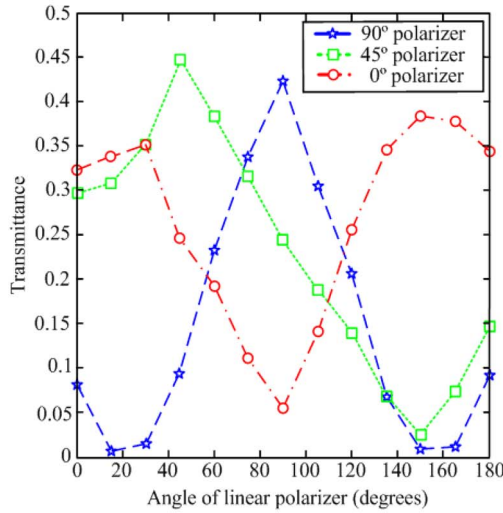
### B. Performance of the Wire-Grid Polarizer

For the measurements of wire-grid transmittance and an extinction ratio (ER), the transmission axis of the linear polarizer in Fig. 6(b) was varied from 0° to 180° in steps of 15° to vary the polarization angle of the light reaching the image sensor. The measured values are normalized with respect to the intensity obtained at the intensity sensitive pixel to compensate for any variation in light intensity and pixel sensitivity over the entire imaging array. The normalized output is the transmittance of the wire-grid polarizer. Normalized transmittance as a function of the transmission axis of the linear polarizer (i.e., the incident polarization angle) for the two polarization sense regions is shown in Fig. 8.

The mean maximum ( $T_{\text{max}}$ ) and minimum ( $T_{\text{min}}$ ) transmittance values for the 0° and 90° polarization sensitive pixels



(a)



(b)

Fig. 8. (a) 0° and 90° polarization profiles in polarization sense region 1. (b) 0°, 90° and 45° polarization profiles in polarization sense region 2.

TABLE III  
TRANSMITTANCE (IN PERCENTAGE) AND ERS

Region	T <sub>max</sub> (0°)	T <sub>min</sub> (0°)	T <sub>max</sub> (90°)	T <sub>min</sub> (90°)	ER
1	0.389	0.07	0.444	0.01	6.3
2	0.384	0.0545	0.424	0.06	7.7

in polarization regions 1 and 2 along with the respective ER achieved for an incident wavelength of 550 nm are shown in Table III. The ER is defined as the ratio of the maximum and minimum transmittance.

The maximum and minimum transmittance for the 45° sensitive pixel in the polarization sense region 2 are 0.446 and 0.02, respectively, producing an extinction ratio of 22. The absorption of the EM waves to completely polarize a transmitted wave through the wire grid is dependent on the pitch of the wire grid; therefore, the ER also varies with the pitch. The chosen technology allows only for a pitch of 480 nm, although less than 300 nm is desired to obtain a high ER value. As the technology scales down, it would allow for a smaller pitch, increasing the ER and, thus, the sensitivity of the polarization applications.

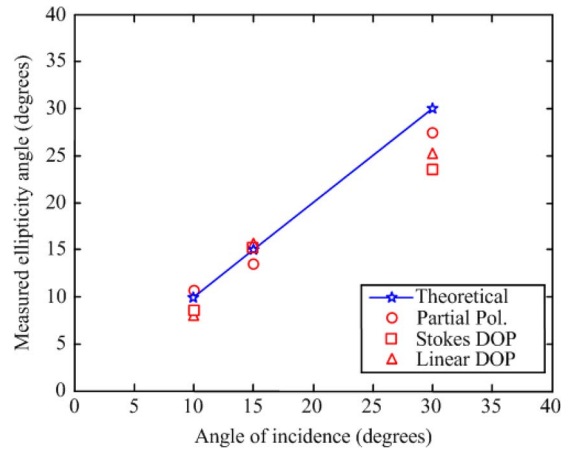


Fig. 9. Measurement of the incident elliptical light ray angle.

Furthermore, the ER is also dependent on the wavelength of incident light.

### C. Incoming Light Ray Direction Detection Using the Ellipticity Angle

To measure the ellipticity angle projected by the incoming light ray, the angular position of the dc light source in Fig. 6(b) was varied to change the incoming light ray direction. Using (4) and (5), the ellipticity angle can be expressed as

$$\chi = \frac{1}{2} \sin^{-1} \left( \frac{S_3}{\delta * S_0} \right) \quad (11)$$

where  $\chi$  is the ellipticity angle, and  $\delta$  is the DOP. The variation in the measured ellipticity angle with the variation in the angular position of the dc light source is shown in Fig. 9.

The ellipticity angle, as shown in (11), depends on the DOP. The measured ellipticity angle for 10°, 15°, and 30° incidence, where the DOP is computed using (5), is shown as the “Stokes DOP” in Fig. 9. The computation of the Stokes DOP from the Stokes parameters needs squaring and square root arithmetic operations. These operations are relatively difficult to implement on-chip.

The calculated ellipticity angle using partial polarization computed from (7) is shown as “partial polarization” in Fig. 9. This computation is easier to implement on-chip as it would only need a differential amplifier to compute the difference and an analog divider.

In sky light polarization, only the linear component of polarization is dominant, and the circular and elliptical components of polarization are usually absent. Thus, for experiments under an open sky, we would be measuring only the linear DOP. The measurement of the ellipticity angle using the Stokes DOLP as in (6) is shown in Fig. 9 as the “linear DOP.”

Correlation coefficients of 0.98, 0.94 and 0.97 are obtained between the theoretical and measured results for the Stokes DOP, partial polarization, and the linear DOP, respectively. The high values of the correlation coefficients imply a strong correlation between the theoretical and measured results.



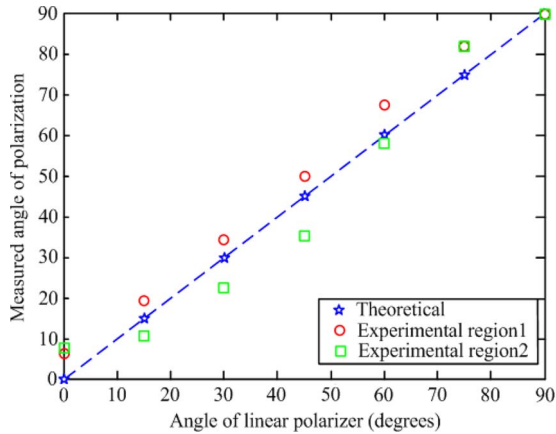


Fig. 10. Measured polarization angle in polarization sense regions 1 and 2.

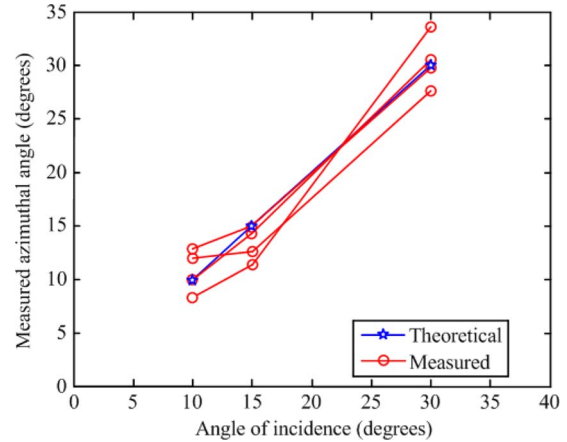


Fig. 11. Measurement of the incident azimuthal light ray angle.

#### D. Incoming Light Ray Direction Detection Using the Azimuthal Angle

The azimuthal angle in sense regions 1 and 2 [see (4)] or, equivalently, the polarization angle measured while varying the transmission axis of the linear polarizer, is shown in Fig. 10.

The correlation coefficient between the theoretical and measured results for regions 1 and 2 are 0.9944 and 0.961, respectively. The high values of the correlations coefficients indicate a strong correlation between the theoretical and measured results. A linear fit error for the measured angle of linear polarization is computed to be 2.3% and 1.1% in sense regions 1 and 2, respectively. For a similar configuration using an organic micropolarizer, the error is reported to be 2.2% [16] and an error of 1.6% using an aluminum nanowire with a wire-grid pitch of 70 nm [23]. The organic micropolarizer exhibits a very high ER; thus, polarization intensity measurements are more accurate. These are, however, very specialized processes and need additional fabrication steps, whereas our method uses only the standard CMOS technology processing steps and produces comparable results.

The measured azimuthal angles for the different angular positions of the dc light source in Fig. 6(b) are shown in Fig. 11. Similar to ellipticity angle measurements, the angular position of the light source and, hence, the angle of incidence of light, was varied by 10°, 15° and 30°. A mean correlation coefficient of 0.9904 is obtained between the theoretical and four measured results.

#### E. DOP Variation With the Angle of the Linear Polarizer

Fig. 12 shows the variation in the Stokes DOLP calculated from (6) and the DOP calculated using the maximum and minimum transmittance [see (7)] with the polarization angle of the incoming light ray. The graph shows the inverse relationship between the orientation angle or the angle of the linear polarizer and the DOLP.

Fig. 12 shows that the DOLP obtained either by the Stokes parameters or by the maximum and minimum transmittance varies from +1 to -1 as the polarizer angle is varied from 0° to 90°. The variation obtained in the DOLP with respect to

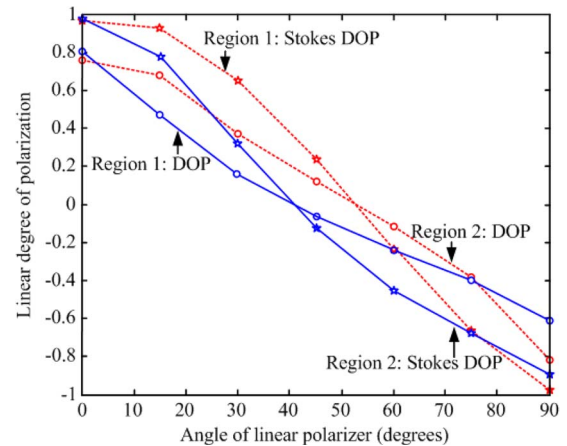


Fig. 12. Degree of linear polarization for sense regions 1 and 2.

the orientation angle can be used as a compass. The proposed model also allows on-chip computations of the DOP, which would make the system simpler and miniaturizable.

## V. CONCLUSION

A CIS with an embedded metallic wire-grid micropolarizer created using the metal layer of a standard CMOS process to detect the incoming light ray direction using the polarization state of incident light is presented. The Stokes parameters used to compute the ellipticity and azimuthal angles of the incoming light ray can be computed on-chip and are shown to be correlated to the incoming light ray direction. A correlation coefficient of over 0.94 was obtained in all measurements. This potential can be used as a compass for navigational algorithms, saving computational power. Furthermore, the DOP was shown to vary with the polarization of the incoming-light-ray direction, which could serve as a compass for autonomous agent navigation algorithms.

The computational algorithms are simplified for on-chip computations, which would result in miniaturized navigational sensors. Such a navigational sensor would be independent of the visual cues and use natural light to determine the directional reference. In the future, these digital algorithms would be

further simplified at the pixel level; interpixel and intrapixel communications to determine the motion and the distance of travel will be implemented and finally will be tried on with mobile autonomous agents.

#### ACKNOWLEDGMENT

The authors would like to thank DALSA for providing the test table to characterize the sensor, Industrial Training in Microelectronics (INVOME) for helping with the fabrication of the chip, and A. Mierop of DALSA, G. Meynants of CMOSIS, and P. Merken for their valuable contributions to the project.

#### REFERENCES

- [1] V. V. Hafner, *Adaptive Navigation Strategies in Biorobotics: Visual Homing and Cognitive Mapping in Animals and Machines*. Aachen, Germany: Shaker Verlag, 2004.
- [2] R. Wehner, B. Michel, and P. Antonsen, "Visual navigation in insects: Coupling of egocentric and geocentric information," *J. Exp. Biol.*, vol. 199, no. 1, pp. 129–140, 1996.
- [3] M. Müller and R. Wehner, "The hidden spiral: Systematic search and path integration in desert ants, *Cataglyphis fortis*," *J. Comput. Physiol. A*, vol. 175, no. 5, pp. 525–530, Nov. 1994.
- [4] Z. Chen and S. T. Birchfield, "Qualitative vision based mobile robot navigation," in *Proc. IEEE Int. Conf. Robot. Autom.*, 2006, pp. 2686–2692.
- [5] G. N. DeSounza and A. C. Kak, "Vision for mobile robot navigation: A survey," *IEEE Trans. Pattern Anal. Mach. Intell.*, vol. 24, no. 2, pp. 237–267, Feb. 2002.
- [6] A. Moini, *Vision Chips*. Boston, MA: Kluwer, 2000.
- [7] R. Wehner and M. Mueller, "The significance of direct sunlight and polarized skylight in the ant's celestial system of navigation," *Proc. Nat. Acad. Sci. U.S.A.*, vol. 103, no. 33, pp. 12 575–12 579, Aug. 2006.
- [8] C. C. Liebe, "Solar compass chip," *IEEE Sensors J.*, vol. 4, no. 6, pp. 779–786, Dec. 2004.
- [9] Y. K. Chang, S. J. Kang, and B. H. Lee, "High accuracy image centering algorithm for CMOS based digital sun sensors," in *Proc. IEEE Sensors Conf.*, 2007, pp. 329–336.
- [10] N. Xie, A. J. P. Theuwissen, and X. Wang, "A CMOS image sensor with row and column profiling means," in *Proc. IEEE Sensors Conf.*, 2008, pp. 1356–1359.
- [11] K. L. Coulson, *Polarization and Intensity of Light in the Atmosphere*. Hampton, VA: Deepak, 1988, p. 2.
- [12] G. S. Smith, "The polarization of skylight: An example from nature," *Amer. J. Phys.*, vol. 75, no. 1, pp. 25–35, Jan. 2007.
- [13] R. A. Richardson and E. O. Hulburt, "Sky-brightness measurements near Bocauiuva, Brazil," *J. Geophys. Res.*, vol. 54, no. 3, pp. 215–227, 1949.
- [14] A. G. Andreou and Z. K. Kalayjian, "Polarization imaging: Principles and integrated polarimeters," *IEEE Sensors J.*, vol. 2, no. 6, pp. 566–576, Dec. 2002.
- [15] X. Zhao, F. Boussaid, A. Bermak, and V. G. Chigrinov, "Thin photo-patterned micropolarizer array for CMOS image sensors," *IEEE Photon. Technol. Lett.*, vol. 21, no. 12, pp. 805–807, Jun. 2009.
- [16] V. Gruev, J. Spiegel, and N. Engheta, "Integrated polarization image sensor for cell detection," in *Proc. Int. Image Sensor Workshop*, 2011.
- [17] E. Hchet and A. Zajak, *Optics*, 3rd ed. Reading, MA: Addison-Wesley, 1988.
- [18] P. B. Catrysse and B. A. Wandell, "Integrated color pixels in 0.18  $\mu\text{m}$  complementary metal oxide technology," *J. Opt. Soc. Amer. A, Opt. Image Sci.*, vol. 20, no. 12, pp. 2293–2306, Dec. 2003.
- [19] M. Sarkar, D. San Segundo, C. van Hoof, and A. J. P. Theuwissen, "Integrated polarization analyzing CMOS image sensor for detecting incoming light ray direction," in *Proc. IEEE Sensors Appl. Symp.*, Feb. 2010, pp. 194–199.
- [20] L. B. Wolff, "Polarization based material classification from specular reflection," *IEEE Trans. Pattern Anal. Mach. Intell.*, vol. 12, no. 11, pp. 1059–1071, Nov. 1990.
- [21] *Xilinx Virtex-II Pro and Virtex-II Pro X FPGA User Guide*, Xilinx, San Jose, CA, 2007. [Online]. Available: [http://www.xilinx.com/support/documentation/user\\_guides/ug012.pdf](http://www.xilinx.com/support/documentation/user_guides/ug012.pdf)
- [22] *AD921:12-Bit 40MSPS Image Signal Processor, Datasheet Rev0*, 2002. [Online]. Available: [http://www.analog.com/static/imported-files/Data\\_Sheets/AD9821.pdf](http://www.analog.com/static/imported-files/Data_Sheets/AD9821.pdf)
- [23] V. Gruev and R. Perkins, "A 1 MPixel CCD image sensor with aluminum nanowire polarization filter," in *Proc. IEEE Int. Symp. Circuits Syst.*, 2010, pp. 629–632.



**Mukul Sarkar** (S'10) received the B.E. degree from Andhra University, Visakhapatnam, India, in 2002 and the M.Sc. degree from the Aachen University of Technology, Aachen, Germany, in 2006. He is currently working toward the Ph.D. degree with the Electronics Instrumentation Laboratory, Faculty of Electrical Engineering, Mathematics and Computer Science, Delft University of Technology, Delft, The Netherlands, with Professor A.J.P. Theuwissen on the subject of biologically inspired complementary metal–oxide–semiconductor image sensors.

From 2003 to 2005, he was with the Philips Institute of Medical Information, Aachen, as a Research Assistant in the detection and analysis of biosignals. His current research interests include biologically inspired vision systems for motion detection and navigation.



**David San Segundo Bello** (M'98) received the M.Sc. degree from the Autonomous University of Barcelona, Barcelona, Spain, and the Ph.D. degree from the University of Twente, Enschede, The Netherlands.

His Ph.D. topic was about the design of pixel-level analog-to-digital converters (ADCs) for hybrid X-ray detectors. He did this work in collaboration with the Dutch Institute of High Energy Physics (NIKHEF) and the European Organization for Nuclear Research (CERN). From 2004 and 2008, he was a Design Engineer with the Wireline Group, Infineon Technologies (currently Lantiq), where he was involved in the design of line drivers and ADCs for x digital subscribe line applications. Since 2008, he has been with Imec, Leuven, Belgium, and has been working on the design of electronic systems and integrated circuits for image sensors. His current research interests include image sensor systems, high-resolution data converters, and complementary metal–oxide–semiconductor sensor readout electronics.



**Chris van Hoof** (M'91) received the Ph.D. degree in electrical engineering from the University of Leuven, Leuven, Belgium in 1992.

In 1998, he became the Head of the Detector Systems Group, Imec, Leuven. In 2002, he became the Director of the Department of Microsystems and Integrated Systems, Imec. In 2007, he became the Program Director of Smart Implants, Imec. In 2009, he became the Program Director of the HUMAN++ Program, Holst Centre, Eindhoven, Netherlands. Since 2002, He has also been with the University of Leuven. He is the author or coauthor of over 250 publications. His research interests include the design, technology, and applications of body area networks and heterogeneous integration for medical and imaging applications.





**Albert J. P. Theuwissen** (M'82–SM'95–F'02) was born in Maaseik, Belgium, on December 20, 1954. He received the M.S. and Ph.D. degrees in electrical engineering from the Catholic University of Leuven, Leuven, Belgium, in 1977 and 1983, respectively.

From 1977 to 1983, his work with the Department of Electrical Engineering (ESAT) Laboratory, Catholic University of Leuven, focused on linear charge-coupled device image sensors. In 1983, he joined the Micro-Circuits Division, Philips Research Laboratories, Eindhoven, The Netherlands, and was involved in research in the field of solid-state imaging, which resulted in the project leadership of standard- and high-definition television imagers. In 1991, he became the Department Head of the Imaging Devices Division, Philips Research Laboratories. In March 2001, he became a part-time Professor with the Delft University of Technology, Delft, The Netherlands, and, since then, has been teaching courses in solid-state imaging and coached Ph.D. students on complementary metal-oxide-semiconductor image sensors. In 2002, he joined DALSA Corporation as the Chief Technology Officer and continued to be its Chief Scientist after retirement from DALSA Corporation. In 2006, he cofounded ImageSensors, Inc. (a nonprofit entity) to address the needs of the image sensor community. In 2007, he started his own company, Harvest Imaging, which focuses on consulting, training, teaching and coaching in the field of solid-state imaging technology. He is the author or coauthor of over 120 technical papers and of the book *Solid-State Imaging with Charge-Coupled Devices* (Boston, Massachusetts: Kluwer Academic Publishers, 1995). He is also a holder of several patents.

Dr. Theuwissen was a member of the Paper Selection Committee, International Electron Devices Meeting, in 1988, 1989, 1995, and 1996. He is a member of the Society of Photographic Instrumentation Engineers. In 1998 and 2007, he became an IEEE Electron Devices and Solid-State Circuits Society Distinguished Lecturer. He was the acting General Chair of the IEEE International Workshop on Charge-Coupled Devices and Advanced Image Sensors in 1997, 2003, and 2009. He is a member of the Steering Committee of the aforementioned workshop and founder of the Walter Kosonocky Award, which highlights the best paper in the field of solid-state image sensors. He is the Coeditor of the IEEE TRANSACTIONS ON ELECTRON DEVICES special issues on solid-state image sensors in May 1991, October 1997, January 2003, and November 2009, and of the *IEEE Micro* special issue on digital imaging in November and December 1998. He is a member of the editorial board of *Photonics Spectra*. Since 1999, he has been a member of the Technical Committee of the International Solid-State Circuits Conference for which he acted as a Secretary, the Vice Chair, and the Chair in the European International Solid-State Circuits Conference (ISSCC) Committee and also a member of the overall ISSCC Executive Committee. Recently, he has been elected to be the International Technical Program Chair, and the Vice Chair and the Chair for the ISSCC 2009 and ISSCC 2010, respectively. In 2008, he received the Society of Motion Picture and Television Engineers' Fuji Gold medal for his contributions to research in the field of solid-state imaging.